Thermochimica Acta 497 (2010) 85–95

Contents lists available at ScienceDirect

Thermochimica Acta

journal homepage: www.elsevier.com/locate/tca

Effect of hydrofluoric acid treatment on the crystallisation behaviour of Zr–Ti–Cu–Al–Ni metallic glass

Jérôme Paillier*, Annett Gebert

IFW Dresden, Postfach 270116, 01171 Dresden, Germany

ARTICLE INFO

Article history:
Received 28 May 2009
Received in revised form 11 August 2009
Accepted 25 August 2009
Available online 1 September 2009

PACS:
81.05.Kf
81.65.Cf
64.70.dg
61.05.cp
68.37.Hk

Keywords:
DSC
Metallic glass
Surface treatment
Crystallisation kinetics
Microstructure
Nucleation

ABSTRACT

The surface of the metallic glass $Zr_{59}Ti_3Cu_{20}Al_{10}Ni_8$ has been modified by hydrofluoric acid (HF) etching treatment. The devitrification and crystallisation process has been mainly studied by isothermal differential scanning calorimetry (DSC), X-ray diffractometry (XRD) and scanning electron microscopy (SEM). The nucleation-growth process is the mechanism of crystallisation; nevertheless the JMA-model is not applicable in every situation. Alternative methods are used to interpret the data. Results show the devitrification process is strongly affected by surface nucleation, which depends on the surface topology. Zr_3Al_2 is the first phase formed on the concave areas whereas the quasicrystalline and Zr_2Ni-based phases appears in the flatter ones. Nevertheless, the presence of an oxide surface layer acts upon the surface nucleation and dwarfs the consequences of such topological differences. Moreover, the quasicrystalline formation appears also to be in competition with the parallel formation of ZrO_2 due to thermal re-oxidation during the DSC experiments.

1. Introduction

In the last 20 years many families of amorphous alloys, among others on Zr-base, have been developed with wide supercooled regions and high-glass forming ability (GFA) [1,2]. The thermal stability range of the supercooled liquid is related to the resistance against crystallisation upon heating and implies from a technological point of view that the material can be easily shaped. On the other hand, the GFA is the ability of a liquid to vitrify upon cooling; the greater the GFA, the lower the cooling rate to obtain a glassy solid. Hence thermal analyses, usually differential scanning calorimetry, are obviously needed for characterisation of amorphous alloys (for example for Zr–Ti–Cu–Al–Ni alloys see Refs. [3–9]).

The preparation of the amorphous alloy Zr–Al–Ni reported in 1990 [10] pioneered the development of the Zr-based alloy family. The addition of copper [11,12] has enabled the preparation of Zr–Cu–Al–Ni alloys in a bulk form, *i.e.* with dimension larger than 1 mm. The small addition of titanium improves the GFA and the critical cooling rate for Zr–Ti–Cu–Al–Ni alloys is in the order of $10\,K\,s^{-1}$ [5,9,13,14]. On the other hand, the effect of Ti on the thermal stability as well as the crystallisation path is strongly dependent on the Ti content [5,9,15,16]. For instance, Kühn et al. [9] have shown that for $Zr_{62-x}Ti_xCu_{20}Al_{10}Ni_8$ alloy icosahedral quasicrystallites appear during the thermal crystallisation only for Ti in the range ($2 \le x \le 4$). Kim et al. [17] have claimed that Ti neither increases the icosahedral short-range order in the liquid nor improves glass formation, but Ti would inhibit surface heterogeneous crystallisation during solidification. It has been demonstrated that crystallisation of metallic glasses of various type can proceed at the surface in a different way than in the bulk [18–20]. Besides, gaining some insight into the surface of amorphous alloys and its related properties, *e.g.* corrosion [21,22] or tribology properties [23], is essential for their industrial expansion. Moreover, as for oxide glass, surface crystallisation might improve the mechanical properties [24].

In this paper, we investigate the influence of the surface on the thermal crystallisation of the amorphous alloy $Zr_{59}Ti_3Cu_{20}Al_{10}Ni_8$. For that purpose, the surface has been modified by chemical way immersing the samples in a strongly diluted hydrofluoric acid solution (HF). Moreover, HF treatment is known to increase the yield of electrochemical hydrogen absorption of Zr-based glassy alloy [25,26]. HF can also be used to modify the surface of metallic glass and increase their catalytic activity as demonstrated for Cu–Zr,

---

* Corresponding author. Tel.: +49 351 4659 872; fax: +49 351 4659 541.
E-mail address: j.paillier@ifw-dresden.de (J. Paillier).

0040-6031/$ – see front matter © 2009 Elsevier B.V. All rights reserved.
doi:10.1016/j.tca.2009.08.014

Cu–Ti or Zr–Ni-based amorphous alloys [27–30]. The changes in properties are commonly attributed to morphological changes of the surface, in particular the removal of the surface Zr/Ti-oxide layer and in parallel the segregation and formation of clusters of the late transition metals (Cu, Ni). Radliński and Calka [31] and Varga et al. [32] reported on the effects of common surface preparation treatments, such as chemical etching or mechanical polishing, upon the thermal behaviour of Zr-based amorphous alloys. We should also mention the works of Köster and Jastrow [33] and Murty et al. [34] on the impact of surface oxidation on the crystallisation process.

As mentioned by many authors, the understanding of the actual mechanism of a thermal process only from thermal analyses and their describing models is an arduous work. The central theme of this report is to set thermal analyses (from differential scanning calorimetry (DSC)) against structural characterisations from X-ray diffractometry (XRD) and scanning electron microscopy (SEM). The process studied is the crystallisation sequence of the glassy alloy $Zr_{59}Ti_3Cu_{20}Al_{10}Ni_8$. It is highlighted how it can be controlled by the surface, through the nucleation process. It is interesting to have in mind the following excerpt from a Zanotto and Fokin's review [35] about surface nucleation in silicate glasses: "Glasses having a reduced glass-transition temperature T_{gr} [temperature of glass-transition normalised to the liquidus temperature] higher than 0.58–0.60 display only surface (mostly heterogeneous) crystallisation, while glasses showing internal homogeneous nucleation have $T_{gr} < 0.58–0.60$". According to this criterion and assuming that it can be extended to metallic glasses, the surface crystallisation of the studied alloy $Zr_{59}Ti_3Cu_{20}Al_{10}Ni_8$ ($T_{gr} = 0.61$) should be significant.

2. Experimental

2.1. Alloy preparation and hydrofluoric acid treatment

The studied amorphous alloy with the nominal atomic composition: Zr (59%), Ti (3%), Cu (20%), Al (10%) and Ni (8%) was prepared in ribbon shape in two steps. The first step was the preparation of a pre-alloy ingot by melting elementary powders in an electric arc furnace under argon atmosphere. The ingot was melted three times for homogenisation. The second step was the preparation of the amorphous alloy itself by melt-spinning. For that, small pieces of the pre-alloy ingot were put in a quartz tube that is placed in the vacuum chamber of the melt-spinner. The tube had been heated up to *ca.* 1500 K and the melted pre-alloy was throwing onto a spinning Cu-wheel (radial velocity: $22\,m\,s^{-1}$) through a slit by an argon stream. By this way, the molten alloy is cooled at rate of *ca.* $10^6\,K\,s^{-1}$. In our conditions and for about 7 g of pre-alloy, we can obtain about 2 m of good quality ribbon (width: *ca.* 5 mm, thickness: *ca.* 40 μm). For this part of the ribbon, the DSC traces (see below) of pieces taken at both ends and in the middle are extremely similar. The surface of the ribbons is not smooth, some features coming with the preparation such as scratches or "bowl-like missing parts" for example due to air trapping between the Cu-wheel and the melt, are present on the surface.

The composition determined by Inductively Coupled Plasma Optical Emission Spectrometry (ICP-OES) is very close to the nominal composition. The oxygen, which can play a big role in the thermal crystallisation of Zr-based metallic glass [7,14,36], is present at a very low level. The determined oxygen mass fraction by hot gas extraction (C436 LECO) for the ribbon is $w_O = 4.3 \times 10^{-4}$.

The hydrofluoric acid (HF) treatments were performed using a solution of 0.1% v/v. This etching agent was prepared from a commercial solution of 38–40% HF (Merck). The samples had been immersed for a defined time ranging from 60 to 240 s before thermal analyses were carried out. The samples are designated as follows: "AS" for the untreated as-spun ribbon; HF60, HF120, HF150, HF180, HF240 for the HF-treated ribbons according to the treatment duration, *i.e.* 60, 120, 150, 180 and 240 s, respectively. The interval between the treatment and the start of the following analyses was about 15 min.

2.2. Differential scanning calorimetry (DSC)

Constant rate heating and isothermal DSC experiments were performed in flowing argon using a power-compensated DSC (Perkin Elmer DSC 7). Each sample had a mass of about 15 mg and was cut in pieces of about $3\,mm^2$ and placed in an Al_2O_3 crucible. The constant heating rate experiments were performed with an average heating rate (β) of $20\,K\,min^{-1}$ and followed by a second heating run (after cooling) under the same conditions. This second scan was used as baseline and subtracted from the first scan. For isothermal experiments, the linear baseline was drawn from the flat signal at the end of the reaction considered.

From constant heating rate experiments were obtained: $T_{e,g}$ (hereafter referred to as the glass-transition temperature T_g) the temperature associated to the extrapolated onset of the endothermic glass-transition event; $T_{e,x}$ (hereafter referred to as the crystallisation temperature T_x) the temperature associated to the extrapolated onset of the crystallisation event. When necessary a second subscript was added to differentiate between different crystallisation events. Moreover, the same label was used to identify the event concerned and an *i* was added at the beginning to identify the related event occurring during isothermal treatment. For instance, T_{x1} was the onset temperature of the event $x1$ and $ix1$ was the related event for isothermal experiments. Two events were considered to be related if their resulting products identified by X-ray diffractometry had been similar.

2.3. Structural characterisation

X-ray diffraction (XRD) analyses were performed using a Philips 1050 diffractometer (Co-Kα radiation, $\lambda = 0.17902$ nm). Diffraction diagrams were collected in the 2θ range from 30 to 95° with a scan rate of $20^\circ\,h^{-1}$. Their analysis and refinement had been carried through the use of the software Powder Cell for Windows v2.4 (Federal Institute for Materials Research and Testing, BAM Berlin, Germany).

The SEM images were obtained using the secondary electron mode of a high resolution scanning electron microscope LEO (Zeiss) 1530 Gemini.

3. Theory

Let α be the expression of the extent to which a reaction has proceeded at a given time t. α is generally expressed as a conversion fraction evolving monotonically between 0 and 1 for the beginning and the end of the reaction considered, respectively. $d\alpha/dt$ is the reaction rate at a given time t and formalised by

$$\frac{d\alpha}{dt} = A\exp\left(-\frac{Ea}{RT}\right)f(\alpha) \tag{1}$$

where R is the gas constant, T is the absolute temperature, A is the pre-exponential factor, Ea is the Arrhenius activation energy and (as A) should not vary with T and $f(\alpha)$ is a function in the differential form depending on the kinetic model.

For isothermal differential scanning calorimetry, α is defined by

$$\alpha(t) = \frac{\Delta_r H(t)}{\Delta_r H(t_f)} \tag{2}$$

and

$$\Delta_r H(t) = K(T)\int_{t_i}^{t} \Delta\varphi \, dt' \qquad (3)$$

where $\Delta_r H(t)$ is the enthalpy released for the reaction considered at the reaction coordinate t, t_i and t_f are the initial and completion time for the reaction considered respectively, $K(T)$ is a temperature-dependent factor depending on the instrument, $\Delta\varphi$ is the monitored massic heat flow rate difference between the sample and reference sides. The integral term of Eq. (3) is determined from the integration of the corresponding peak on the DSC curve.

On the other hand, the integration of Eq. (1) leads to

$$g(\alpha) = \int_0^{\alpha} \frac{d\alpha'}{f(\alpha')} = kt \qquad (4)$$

where $g(\alpha)$ is the integral form of the reaction model, k is the reaction rate constant and

$$k = A\exp\left(-\frac{Ea}{RT}\right) \qquad (5)$$

The master plot of a reaction model is a curve depending only of the reaction model considered (and independent of the value of the input parameters of the model). Under isothermal conditions, the master plot based on the integral form is the plot of $g(\alpha)/g(0.5)$ against α (where $g(0.5)$ is the value of $g(\alpha)$ for $\alpha = 0.5$); moreover (see Ref. [37] for details):

$$\frac{g(\alpha)}{g(0.5)} = \frac{t}{t_{0.5}} \qquad (6)$$

where $t_{0.5}$ is the time corresponding to $\alpha = 0.5$. Hence, by comparison between the different master plots of the existing models and the plot of $t/t_{0.5}$ against α (easily obtained from experimental data) the right reaction model to apply can be recognized.

$f(\alpha)$ and $g(\alpha)$ embody a kinetic model and is either a mathematical expression for a well-defined process, a reaction model, or an algebraic expression defined empirically. Many reaction models exist, for example based on diffusion or nucleation-growth processes [38]. Among those, the models A2 and A3 considering a two- or three-dimension nucleation-growth process can be cited:

$$A2: g(\alpha) = [-\ln(1-\alpha)]^{1/2} \qquad (7a)$$

$$A3: g(\alpha) = [-\ln(1-\alpha)]^{1/3} \qquad (7b)$$

On the other hand, in the field of all solid-state reactions the so-called 'JMA model' (or JMAEK in reference to Johnson, Mehl, Avrami, Erofeev and Kolmogorov, respectively) based on the triad nucleation-growth-impingement and its various theoretical and empirical extensions are beyond any doubt the most used [39,40]. A possible expression is as follows:

$$f(\alpha) = m(1-\alpha)[-\ln(1-\alpha)]^{1-1/m} \qquad (8)$$

where m is called the kinetic exponent. The formalism has been obtained by considering the constrained nature of a solid-state reaction, with some assumption on the nucleation rate and the growth rate. It is essentially a geometrical problem and thus the kinetic exponent m of Eq. (8), generally an integer or a half-integer, depends on the geometrical nature of the growth mode that takes place. Nevertheless, the only determination of m from an experimental set of data by means of Eq. (8) does not give enough information to ascertain the growth behaviour.

The assumptions that inhere in the described formalism are of two kinds. Some of them enable the statement of the basic Eqs. (1) and (2) whereas others delimit the validity of kinetic models. Their suitability for a particular thermal process can be checked using two special functions, namely the $y(\alpha)$ and $z(\alpha)$ functions [41]. For an isothermal process they are defined as follows and normalised in such a way they are in the interval [0,1]:

$$y(\alpha) = \Delta\varphi \qquad (9a)$$

$$z(\alpha) = \Delta\varphi\, t \qquad (9b)$$

These two functions must be invariant for a process with regard to the experimental variables, which is to say within a temperature range for isothermal experiments. The non-observance can arise from extrinsic factors (data recordings, analyses, etc.) or from intrinsic factors due to a complex process.

Moreover, the two invariant functions, $y(\alpha)$ and $z(\alpha)$, have global maxima at positions α^* defined only by the kinetic model used. For the JMA-model (Eq. (8)) they are [41]:

$$\alpha_Y^* = 1 - \exp(m^{-1} - 1); \quad m > 1 \qquad (10a)$$

$$\alpha_Z^* \cong 0.632 \qquad (10b)$$

The value of α_Z^* is therefore a criterion that can be used first for assessing whether the JMA-model is applicable. To our knowledge only Lad et al. [42] and Wang et al. [43] have used it to study the kinetic data of crystallisation of metallic glasses under non-isothermal conditions.

4. Results and discussion

4.1. Structural characterisation and survey of the thermal crystallisation behaviour

4.1.1. Structural characterisation after HF treatment

The amorphous nature of the samples has been checked by XRD and transmission electron microscopy (TEM) in addition to the constant heating rate DSC curves presented below. Diffraction diagrams (not shown here) exhibit only humps, which is typical for an amorphous material [3,4,6,8,26]. The patterns for as-spun and HF-treated samples are similar, with the exception of a small peak centred on the position of the most intense Cu peak that appears after etching. TEM analyses (not shown here) before and after HF treatment reveal that the samples are in every instance fully amorphous since no small ordered regions have been detected in the materials bulk. Therefore, the small crystalline regions detected by XRD are located on or close to the surface.

Scanning electron microscopy (SEM) images confirm this. For the sample etched for 60 s (HF60), the surface is covered by Cu-rich lumps of roughly twenty nanometres (size compatible with the width of the XRD peak) with a density of ~200 μm^{-2}. This density (see Fig. 1) increases up to ~1500 μm^{-2} for a sample etched for 120 s (HF120). Nevertheless, for this sample like for samples with longer HF treatments, the regions with Cu-rich lumps appear to be replaced by a new flatter surface (with less Cu-rich lumps) where pitting corrosion occurs (see Fig. 1). After the longest HF treatment studied (HF240), pits (with most abundant pit opening ranging from ~100 to 800 nm in diameter) are homogenously distributed over the whole surface with a density of ~2.5 μm^{-2}.

By energy-dispersive X-ray spectroscopy (EDX), no change can be detected between the spectra of the as-spun and etched samples. Therefore, the composition is globally unchanged after the HF treatment and equal to the nominal one in roughly the first cubic micrometer of the materials. Nevertheless, there is surely a change in the surface composition itself with an enrichment in copper/nickel and a depletion in zirconium [26,28,29] due to a preferential dissolution of this one. The measured density of a sample etched for 240 s is 6.611 g cm^{-3}, that is to say slightly higher than the measured density of the untreated sample. That agrees with a partial dissolution of the less dense elements (Zr, Ti, Al).

Overall, the largest part of the samples is not affected by the applied HF treatment. The structural and chemical changes have

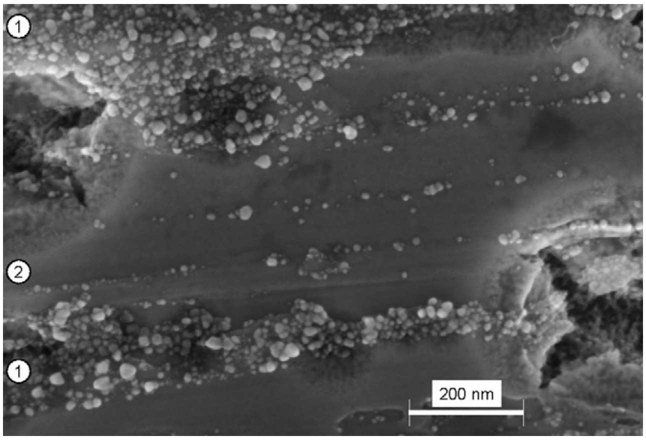

Fig. 1. SEM picture of the surface of the sample immersed 120 s in HF (HF120), this region displays the evolution of the surface microstructure according to the immersion time. The areas tagged 1 are typical of shorter etching time and exhibit Cu-rich lumps, whereas the area tagged 2 develops for longer etching time and flatter surface with corrosion pits appears.

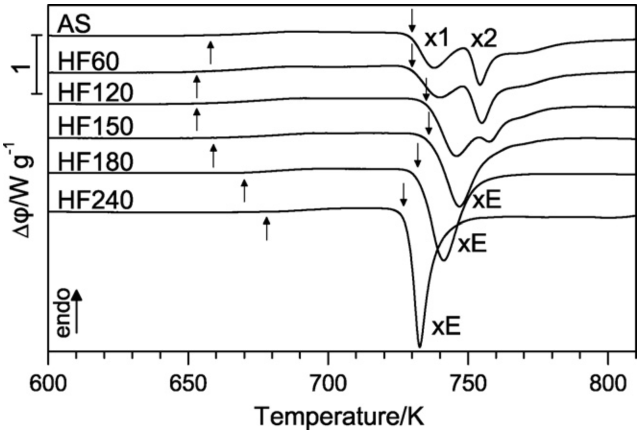

Fig. 2. DSC curves recorded at $\beta = 20\,\mathrm{K\,min^{-1}}$ for as-spun sample (AS) and various etching time from 60 s to 240 s in HF 0.1% v/v; upward and downward arrows indicate T_g and T_x, respectively (see also text and Table 1).

taken place on the very surface itself or in a thin layer below it. The following interpretations of the results are based on these observations.

4.1.2. Constant heating rate DSC

This mode is suitable to survey the sample thermal behaviour in a wide thermal range. The influence of the HF treatments is displayed for temperatures below 800 K in Fig. 2 and Table 1 gives the main parameters of the supercooled liquid region (SLR), *i.e.* the thermal range between the glass transition and the beginning of crystallisation. For the as-spun ribbon, the SLR is 72 K, the crystallisation starts at 730 K and is characterised by two main exothermic peaks called $x1$ ($T_{x1} = 730$ K) and $x2$ ($T_{x2} = 748$ K). A third exothermic event ($x3$) is also discernible overlapping the right tail of $x2$, its maximum temperature is *ca.* 765 K. In the following $x3$ is not considered. The results are similar to those previously published for the same alloy [9].

The implementation of HF treatments of various durations does not lead to monotonic alterations of the SLR. The SLR rises first by 10 K, up to treatment duration of 120 s, and then decreases by 30 K. The changes of apparent T_g and T_x are both responsible of the changes of the SLR. The large variation of T_g is surprising and should be confirmed with a more precise technique before to draw a definite conclusion. The aspect of the monitored DSC traces corresponding to the first sequence of crystallisation (*i.e.* between T_x and 800 K) depends also of the HF treatment duration previously applied to the sample. Two sets of behaviour are recognisable: for short etching duration (*ca.* <60 s), the same exothermic events are present as for the untreated sample ($x1$, $x2$); for longest duration (*ca.* >150 s), on the contrary only one exothermic event (labelled xE) is present. The respective diffractograms obtained after $x1$–$x2$ and xE are different, the former is a mix of quasicrystalline (qc) and Zr_2Ni phases, whereas the latter is composed of Zr_3Al_2 (see below, for more details). In both cases, some minor and unidentified phases are present. For HF treatments close to 120 s, the behaviour is difficult to characterise properly. It appears to be the sum and a transition between the two already defined behaviour. There is no abrupt switch between both crystallisation regimes. Note that when the sample HF150 is kept many weeks in ambient atmosphere after HF treatment, it behaves during the following crystallisation like HF120 since the events $ix1$, $ix2$ reappear and the behaviour appears thus to be the sum of the events $ix1$, $ix2$ and ixE. This is attributed to the re-oxidation of the surface that would neutralise certain regions active for the generation of Zr_3Al_2 (see below, for more details).

On the other hand, there is a second sequence of crystallisation before the alloy starts melting at about 900 K [3]. Fig. 3 (inset: DSC curves in the range 800–950 K; main: diffractograms) displays the corresponding results. From the comparison of diffractograms of as-spun and HF-etched samples (only HF150 is shown), it is obvious that the crystalline products obtained at 950 K are similar regardless of the application and the eventual duration of a HF treatment. The main crystalline phase is based on the tetragonal compound Zr_2Cu (Pearson symbol: tI6, space group: *I4/mmm*, *Strukturbericht*: $C11_b$). Its calculated lattice constants are $a = 0.320$ nm and $c = 1.113$ nm corresponding to shrinkages against the pure compound of 0.6 and 0.4%, respectively. These values match well the lattice constants deduced from the Vegard law considering the substitution solid solution $(Zr_{0.95}Ti_{0.05})_2Cu$, *i.e.* with the same Ti/Zr ratio than the initial amorphous alloy. This point agrees with the isomorphous replacement of Zr by Ti for this class of alloys [44]. On the contrary, the DSC traces corresponding to

Table 1
Summary of the changes in the surface microstructure and in the relevant temperature of the supercooled liquid region (T_g, T_x: apparent glass transition and crystallisation onset temperatures, respectively, $\Delta T = T_x - T_g$) for various samples (AS: as-spun, HF60: etched 60 s, etc.). The DSC main events observed for $T < 823$ K ($\beta = 20\,\mathrm{K\,min^{-1}}$) and the main phases obtained for an upper limit of 823 and 950 K are indicated too.

Sample	Evolution of the microstructure (SEM)	SLR temperature (K)			Events $T < 823$ K	Phases obtained at	
		T_g	T_x	ΔT		823 K	950 K
AS	N/A	658	730	72	$x1$, $x2$	qc + Zr_2Ni	Zr_2Cu
HF60	Cu particles (~20 nm) ~200 μm^{-2}	653	731	78	$x1$, $x2$	qc + Zr_2Ni	Zr_2Cu
HF120	Double microstructure: Cu particles ~1500 μm^{-2}, no Cu particles + pits	653	735	82	mix	Zr_3Al_2	Zr_2Cu
HF150	Pits (100–800 nm)	659	735	76	xE	Zr_3Al_2	Zr_2Cu
HF180	Pits (100–800 nm)	670	732	62	xE	Zr_3Al_2	Zr_2Cu
HF240	Pits (100–800 nm) ~2.5 μm^{-2}	678	728	50	xE	Zr_3Al_2	Zr_2Cu

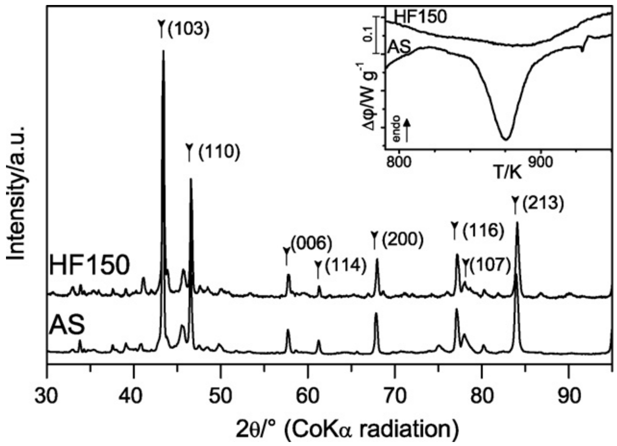

Fig. 3. XRD patterns of the as-spun (AS) and etched 150 s in HF (HF150) samples recorded after heating at $\beta = 20\,\mathrm{K\,min^{-1}}$ up to 950 K. The corresponding DSC scans (for temperature higher than 800 K) are shown in inset. The marks and Miller indices correspond to Zr_2Cu.

the formation of the Zr_2Cu phase at *ca.* 875 K (inset into Fig. 3) are obviously different according to the sample. Their final crystalline products being very similar, it is therefore due to the difference of the reactants, *i.e.* the intermediate products formed at *ca.* 800 K. This point is discussed in more details below.

4.1.3. Isothermal DSC

This mode is suitable to carry out a careful analysis of the kinetic parameters of the process(es) occurring during the reaction considered. We have focused on the first sequence of the crystallisation (*i.e.* between T_x and 800 K) since it is the one delimiting the thermal stability of the glass. Fig. 4 shows the curves obtained for the samples AS, HF60 and HF150 at 725 K. The same division as reported in Fig. 2 appears in the crystallisation process according to the duration of the HF treatment. For AS and HF60, two steps are clearly recognisable. The first one, *ix*1, is completed after *ca.* 200 s whereas the second one, *ix*2, starts about 30 s after the end of *ix*1 and lasts about 300 s. In the sense defined in Section 2, the isothermal events *ix*1 and *ix*2 are obviously related to the events *x*1 and *x*2(−*x*3?) occurring during the constant heating rate experiments. On the other hand, for HF150 only one event, *ix*E, occurs. The event *ix*E is completed after *ca.* 200 s and is related to *x*E. Furthermore, the isothermal behaviour is the same for the samples longer etched (HF180, HF240). The time evolution of the conversion fractions α of the event *ix*1 for the AS and HF60 samples have been inset into Fig. 4. It clearly appears that a longer time is needed for HF60 in comparison to AS to reach a same level of transformation. Such a delay in the crystallisation curve can be interpreted in many ways, for example by a change in the growth velocity or by a transition in the nucleation process from heterogeneous-to-homogeneous and/or from steady-state-to-transient [45] or by a change in the site density. In a phenomenological meaning, this can be seen as a more difficult nucleation (or growth) of the quasicrystalline phase after the sample has been etched for 60 s and consequently its surface modified.

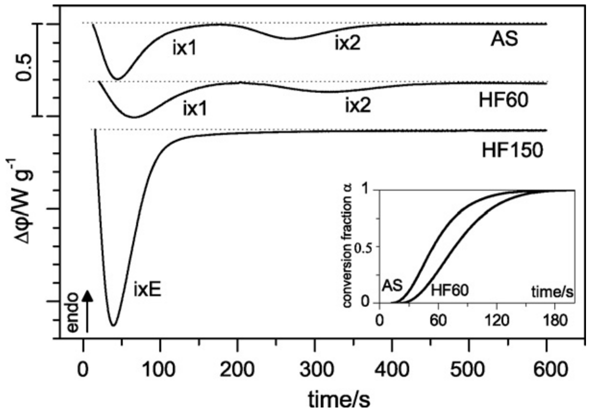

Fig. 4. DSC isothermal curves recorded at $T = 725$ K for the samples: as-spun (AS), etched 60 s or 150 s in HF (HF60, HF150). Inset: evolution of the conversion fraction for the event *ix*1 (quasicrystalline phase formation).

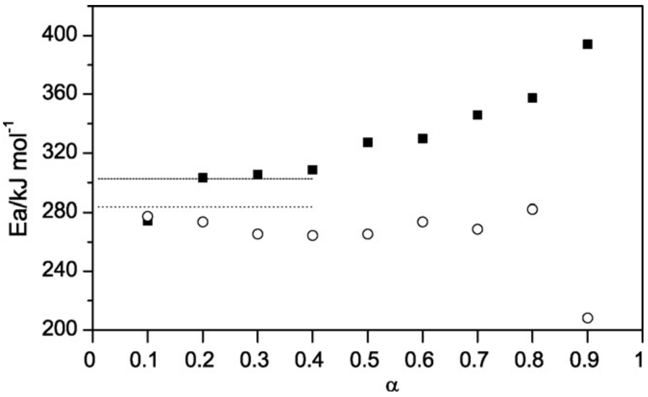

Fig. 5. Activation energy for quasicrystalline phase formation determined from isoconversional method: closed symbols: as-spun sample (AS), open symbols: sample etched 60 s (HF60). The dotted lines represent the corresponding values determined by means of the Arrhenius equation.

At this stage the activation energy $Ea(\alpha)$ can be determined using an isoconversional method through Eq. (11) [41] which allows problems of kinetic model determination to be avoided:

$$Ea(\alpha) = -R\left(\frac{d\ln\Delta\varphi}{dT^{-1}}\right)_{\alpha} \qquad (11)$$

The plots thus obtained for the event *ix*1 for the samples AS and HF60 are shown in Fig. 5. Clearly, the activation energy is almost constant with the degree of advancement of the quasicrystalline phase formation for HF60. On the contrary, there are wide variations in values for the as-spun sample (AS). It is the sign of a more complex mechanism for this sample.

Fig. 6a shows the diffractograms recorded after 180 s of isothermal annealing at 725 K for the samples as-spun (AS) and etched for 60 s (HF60), *i.e.* after the event *ix*1 occurred. The corresponding diffractogram for the sample etched for 150 s (HF150) and annealed for 180 s is not shown since it is analogous to the one obtained after 600 s of annealing and shown in Fig. 6b. Both diffractograms in Fig. 6a are almost identical and can be ascribed to a quasicrystalline (icosahedral) phase. The peaks are less sharp for the HF-treated sample. The indexation of the peaks and the determination of the quasi-lattice constant, *aq*, have been made as previously described [46]. The determined value of *aq* is 0.477 nm in both cases and is similar to the one previously reported [44].

Fig. 6b shows the diffractograms obtained after 600 s of isothermal treatment of the samples AS, HF60 and HF150. For AS, in addition to the quasicrystalline phase, a second phase with the structure of the tetragonal compound Zr_2Ni (Pearson symbol: tI12, space group: *I*4/*mcm*, *Strukturbericht*: C16) is present. Its determined lattice constants are $a = 0.652$ nm and $c = 0.522$ nm. The structure has roughly the same unit cell volume ($V = 222\,\text{Å}^3$) but is slightly distorted compared to the compound Zr_2Ni ($c/a = 0.81$ *vs.* 0.80). For HF150, only one phase with the structure of the tetragonal compound Zr_3Al_2 (Pearson symbol: tP20, space group: $P4_2/mnm$) [47] is present. The structure is strongly shrunk compared to the compound: $a = 0.753$ nm (−1.3%); $c = 0.682$ nm (−2.6%)

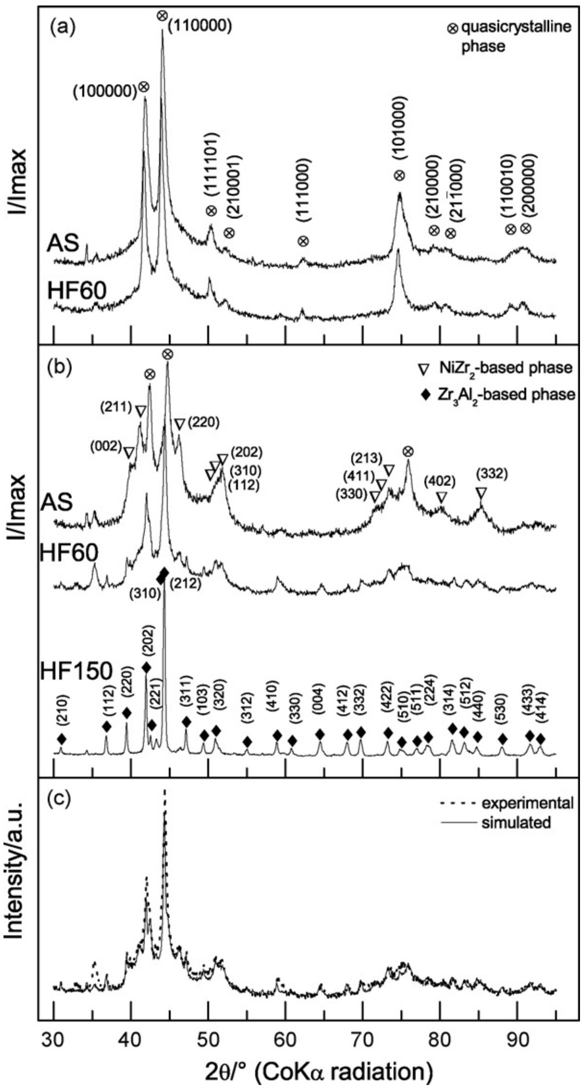

Fig. 6. XRD patterns obtained after isothermal treatment at 725 K for the as-spun sample (AS) and the HF-treated samples during 60 s (HF60) or 150 s (HF150), (a) after180 s, (b) after 600 s and (c) simulation of the pattern for HF60 after 600 s.

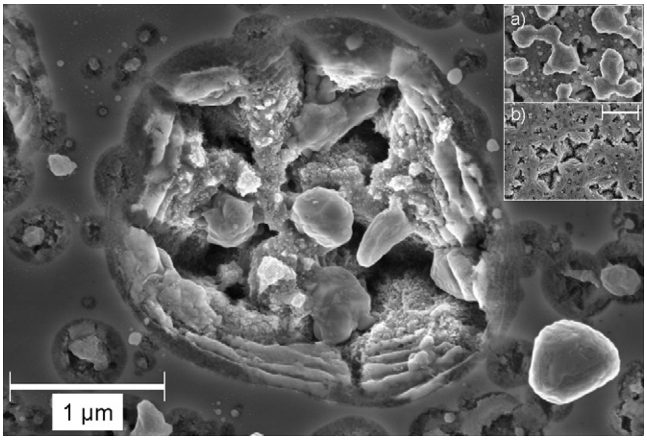

Fig. 7. SEM pictures of the samples etched 240 s (HF240) at the beginning of the crystallisation at 725 K and in inset (a) after completion of the process and (b) picture of the surface before crystallisation.

and $V = 379\,\text{Å}^3$ (−7%). For HF60, the diffractogram can be fitted as a sum of the diffractograms for AS and HF150 as shown in Fig. 6c. Three main phases are therefore present: quasicrystalline, Zr_2Ni- and Zr_3Al_2-based. To our knowledge, a Zr_3Al_2-based phase has been only reported by Yavari et al. [48,49] as involved in the crystallisation process of Zr-based metallic glass. The presence of a quasicrystalline phase makes tough the refinement and the determination of the phase mass fraction.

4.1.4. *Structural characterisation after start of the crystallisation*

This section addresses the main results of the structural characterisation of the surface after the crystallisation process had begun. It has been earlier observed that the Zr_3Al_2 phase appears concurrently with the corrosion pits (Table 1). The direct connection is shown in Fig. 7. The main picture is typical of the early stage of the crystallisation process and exhibits that crystals grow from the inner walls of a corrosion pit towards its open regions. These “first-born” crystals merge to form one secondary polycrystal with the same size than the opening of the pit. In the following, the secondary crystals continue to grow towards the outside of the pits. Each secondary crystal originating from an individual corrosion pit swell and finally can join some of its neighbours to form tertiary crystals. The inset (a) of Fig. 7 shows this kind of tertiary crystals of Zr_3Al_2 after 10 min of annealing at 725 K. For the sake of comparison, the inset (b) shows the surface with the same magnification of the same sample before the crystallisation process had been set in motion.

Fig. 8 shows the situation at the beginning of the crystallisation of the sample HF120, *i.e.* etched for 120 s. It has been earlier shown that this sample exhibits a DSC behaviour which is a mix of the “normal” behaviour, *i.e.* for the untreated sample, and the one observed for longest HF treatment, like for HF240. As already shown (Fig. 1), this sample has also a double surface microstructure. In the regions with some corrosion pits, the morphology observed after the begin-

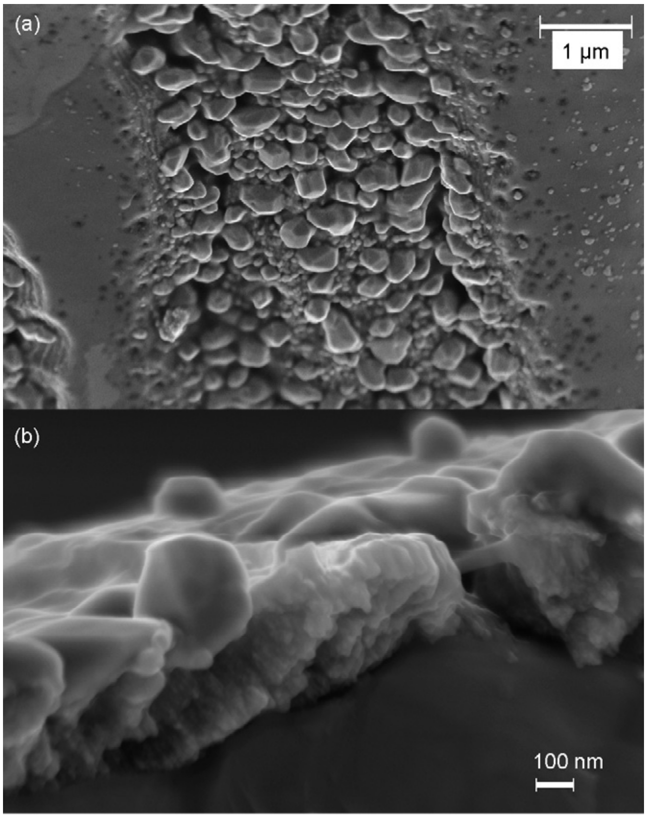

Fig. 8. SEM pictures of the samples etched 120 s (HF120) at the beginning of the crystallisation at 725 K: (a) picture of a trench generated during the melt-spinning preparation of the alloy and (b) cross-section of a region without trench.

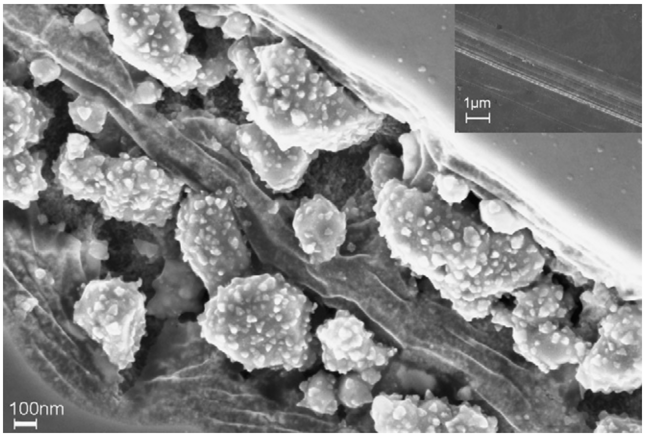

Fig. 9. SEM pictures of the samples etched 60 s (HF60), and in inset of the as-spun ribbon (AS), after 10 min of annealing at 725 K.

ning of the crystallisation is similar to the one for HF240, namely primary crystals growing from the inner walls of the corrosion pits. This morphology is also observed in the trenches that are present on the surface of the ribbon samples (Fig. 8a). These trenches with a width in the micrometer range, and a length that can reach many centimetres, come from the preparation process. In these trenches, as well as for the others "concave features" such as pits, crystals well faceted of many hundreds of nanometres are clearly seen. Crystals with shapes like tetragonal bipyramid or tetragonal prism, that is to say compatible with the symmetries of Zr_3Al_2, are obviously distinguishable. The presence of such relatively big monocrystals agrees with the narrow fwhm of the XRD-peaks of this phase reported above. We can see in Fig. 8b that the crystallised region morphology is different for the other regions of the samples, *i.e.* with morphology of Cu-rich lumps of 20 nm on the surface (area tagged 1 in Fig. 1). Instead of emerging crystals, there is a shapeless crystallised layer on the surface and parallel to it. This layer is assumed to correspond to the quasicrystalline/Zr_2Ni crystallised phase. Some crystalline outgrowths are visible that might be ZrO_2. Note that the Cu-rich lumps initially present cannot be distinguished after crystallisation.

The sample etched for 60 s (HF60) once it has undergone 10 min of isothermal annealing at 725 K contains a Zr_3Al_2-base phase as shown by the XRD pattern (Fig. 6). According to the previous observation, its presence is expected in the concave areas of the ribbon, especially the trenches created by the preparation process. Fig. 9 shows such a region. Crystalline regions grown from the rims of a trench are clearly visible but their morphologies is very different to the previously observed ones. In all likelihood, these crystalline regions are all the same Zr_3Al_2 phase and their dissimilar aspects may be due to different growth modes. The image of such a trench after the same annealing treatment for an as-spun sample (inset in Fig. 9) does not show any feature, which agrees with the XRD pattern of this sample that does not show the formation of the Zr_3Al_2 phase (Fig. 6). It is therefore inferred that the presence of a native oxide on the surface of the samples hinders the development of such emerging crystals and that the crystallisation process develops with a stratified morphology parallel to the surface as shown in Fig. 8b. Note that also for the sample HF60 the Cu-rich lumps created by the HF treatment are not visible anymore.

Taking heed of the whole results, we can infer that the main structural/chemical attributes of the surface acting upon the crystallisation process are the presence (or not) of a naturally formed oxide layer and the presence (or not) of concave regions. On the other hand, the presence of outgrowths, such as the Cu-lumps, does not display any (clear) influence. The concave areas favour the formation of emerging crystals, especially Zr_3Al_2, provided that the native oxide is not present. On the contrary, the presence of this oxide or a flatter topology leads to a stratified morphology parallel to the surface for the crystallised regions, these ones being constituted by quasicrystalline/Zr_2Ni phases. On the atomic level, a critical factor is assumed to be the atomic surface mobility which can be affected by the topology of the surface and its covering by an oxide layer. Further investigations ought to be carried out to fully describe the global crystallisation process and the entire mechanism (nucleation and growth) of the material.

4.2. Kinetic analysis

4.2.1. Check of the validity of the JMA analysis—$y(\alpha)$, $z(\alpha)$ functions

The JMA analysis (Eq. (8)) is the most commonly employed method to deal with kinetic data of crystallisation processes of amorphous alloys. It is therefore important to check the validity of the JMA analysis for the present set of data. The validity can be checked using the $y(\alpha)$ and $z(\alpha)$ functions defined in Eq. (9) [41]. In particular, the maximum of $z(\alpha)$ must appear for α very close to 0.632 (Eq. (10b)) when the JMA-model can apply. On the other hand, the invariant functions $y(\alpha)$ and $z(\alpha)$ can be used to evidence complex mechanism/kinetic processes. Fig. 10 shows several cases for the $y(\alpha)$ and $z(\alpha)$ when applied to our set of data. Firstly, Fig. 10c and d concern the event *ix*2 (Zr_2Ni-based phase formation). Both functions display a simple shape and are invariant with respect to the temperature (705–725 K) as well as the application of a surface treatment (since plots for AS and HF60 are superimposed). Moreover, the position of the maximum of $z(\alpha)$ is in agreement with the JMA-model. Secondly, the situation for the event *ix*1 (quasicrystalline phase formation) shown in Fig. 10a and b is different since the invariance for all the experimental parameters is not preserved, particularly for HF60. The functions are actually invariant for the sample AS but the maximum of $z(\alpha)$, appearing for α of roughly 0.5, indicates the JMA-model is not applicable. For the HF60 sample, the situation depends on the working temperature. For $T \leq 715$ K the situation is similar to the case of AS, but for $T = 725$ K, plots of $y(\alpha)$ and $z(\alpha)$ are different and cannot be superimposed to the previous ones. In particular, the position of the maximum of $z(\alpha)$ matches here the value implied by the JMA-model.

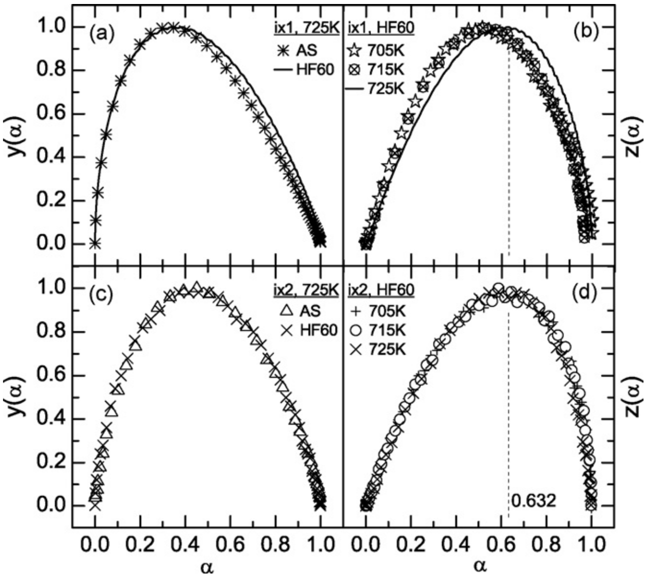

Fig. 10. Comparison of the functions for: event *ix*1 (a) $y(\alpha)$ at 725 K for samples AS and HF60 (b) $z(\alpha)$ for HF60 between 705 K and 725 K and event *ix*2 (c) $y(\alpha)$ at 725 K for samples AS and HF60 (d) $z(\alpha)$ for HF60 between 705 K and 725 K.

It has already been mentioned by many authors that the use of the JMA-model to represent the crystallisation of metallic glasses can be inadequate (*e.g.* [18]) generally due to the impossibility to describe the kinetic data using a unique kinetic exponent m (Eq. (8)). The deviation from the JMA-model may arise from inadequate assumptions about the nucleation, the growth or both. Moreover, the nucleation in the metallic glass can be a complicated and coupled multi-process and not well described by the classical theory as discussed by Kelton [50]. The reason(s) for which the quasicrystalline phase formation can or cannot, according to the situation, be described by the JMA-model has(have) not been fully understood yet. We think the main cause is linked with surface processes. We have observed a strong simultaneity between the validity of the JMA-model and the re-oxidation of the surface during crystallisation (see below).

Recent studies [42,43], leaning on the Eq. (10b), have reported that the crystallisation of metallic glasses can or cannot, according to the heating rate used in non-isothermal DSC, be described by the JMA-model. Lad et al. [42] have proposed a combination of isokinetic and isoconversional methods for interpretation while Wang et al. [43] have described their data with the more general autocatalytic model (Šesták–Berggren equation). The application of the autocatalytic model in our case has led to very good fits for all the considered data in the range $\alpha = 0.2–0.9$. Nevertheless, it is hard to interpret the variation of the two fitting parameters and the reported structural changes tracked by XRD are not strikingly and obviously underlined. Some authors [51–53] have applied an alternative method of examining their data considering that the kinetic exponent of the JMA equation (henceforth called differential or local exponent) is not constant and varies with the degree of advancement of the transformation, namely α. As previously, this method applied to our set of data does not lead to a striking description of the reported structural change.

A global description of the observed phenomena (especially the reported structural change) is better reached using the reaction model as shown in the next part.

4.2.2. Analysis with a reaction model

For that purpose we have looked for a reasonable concordance between our experimental master plots (curves $t/t_{0.5}$) and the theoretical master plot of a model (curves $g(\alpha)/g(0.5)$) according to Eq. (6). The results for the samples AS and HF60 are shown in Fig. 11a and b for the isothermal events *ix*1 and *ix*2, respectively. Assuming that processes occurring for both samples are of identical nature we can ascribe the model A2 (Eq. (7a)) to the event *ix*1 and A3 (Eq. (7b)) to the event *ix*2. Note that for $m = 2$ and $m = 3$, the algebraic expressions of the JMA-model are equivalent to those of the reaction models A2 and A3, respectively. Since we have previously shown than the JMA approach does not work in every situations, the appropriateness of the use of such “equivalent” reaction models is questionable. Our purpose is not to give a kinetic description here, but to interpret the SEM and XRD results by means of the kinetic data. The fact that A2/A3 are based on nucleation/growth mechanism, commonly admitted for this kind of process, and the agreement between the theoretical and experimental master plots can be seen as a justification of this approach.

The use of A2/A3 is equivalent to set a constant growth mode for the nucleation-growth process, in particular to assume an ideal three-dimension growth process. It is obvious for the Zr_2Ni-growth, since the model A3 describes the event *ix*2. We assume it is valid also for the quasicrystalline phase growth, event *ix*1, since according to Ozawa [54], the kinetics of a three-dimension growth process from surface nuclei is represented by a value of 2 for the exponent (as in the formal expression of A2 in Eq. (7a)) and not 3 like for the growth from bulk nuclei. So, we infer the surface plays a role in the quasicrystalline phase formation.

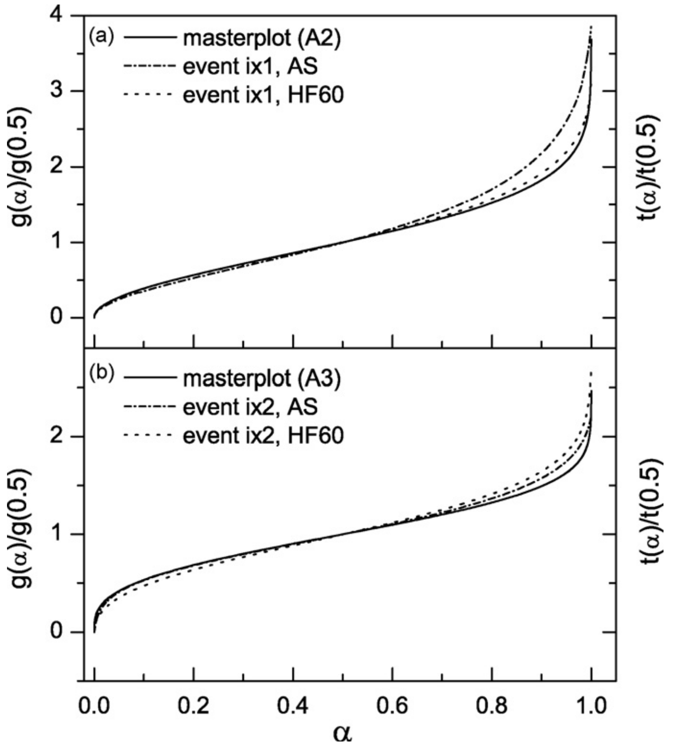

Fig. 11. Comparison of theoretical master plots ($g(\alpha)/g(0.5)$) and experimental master plots ($t(\alpha)/t(0.5)$) obtained form isothermal curves recorded at 725 K for the as-spun (AS) and etched 60 s in HF (HF60) samples: (a) th.: mechanism A2; exp.: event *ix*1 for AS and HF60, (b) th.: mechanism A3; exp.: event *ix*2 for AS and HF60.

Once the kinetic model chosen, the reaction rate constants k can be determined using Eq. (4) and are given in Table 2. Two rate constants are given for each sample and each event. It is not possible for the sample AS and the event *ix*1 to determine an acceptable correlation with a unique rate constant along the whole α range, indeed. Therefore, the whole α range is split. The splitting value is the value of α corresponding to the maximum rate of the reaction. In this way, a reaction rate constant is determined for each subrange with better correlations. For the sake of comparison the same method is applied for each case, despite a good correlation can be obtained with a unique rate constant along the whole α range. It can be deduced from Table 2 that the HF treatment influences strongly and only the kinetics of the beginning of the crystallisation process from the supercooled liquid region leading to the formation of quasicrystals, event *ix*1. On the other hand, the entire process leading to the formation of the Zr_2Ni-phase appears to be retarded after HF treatment, event *ix*2.

Table 2
Reaction rate constants k for the isothermal ($T = 725$ K) events *ix*1 (model A2) and *ix*2 (model A3) and their range of validity as well as the correlation determined with the method of least squares. The split value for the α ranges corresponds to the maximum reaction rate. The samples are the as-spun material (AS) and etched 60 s (HF60).

Event	Sample	k (s^{-1})	α range	Correlation
*ix*1	AS	0.0220	0–0.32	0.9987
		0.0144	0.32–0.99	0.9900
	HF60	0.0151	0–0.34	0.9999
		0.0144	0.34–0.99	0.9980
*ix*2	AS	0.0084	0–0.43	0.9988
		0.0073	0.43–0.99	0.9994
	HF60	0.0068	0–0.48	0.9995
		0.0052	0.48–0.99	0.9982

Table 3
Kinetic triplets in the temperature range 705–725 K for the isothermal events *ix*1 and *ix*2 before and after 60 s HF treatment. Values with a §-superscript are considered to be without physical meanings (see text).

Sample	Event	A ($\times 10^3$ s^{-1})	Ea (kJ mol^{-1})	Model
AS	*ix*1	133×10^{15}	302	A2
HF60	*ix*1	4×10^{15}	284	A2
AS	*ix*2	106×10^{15}	306	A3
HF60	*ix*2	$51^{§}$	$95^{§}$	A3

From a set of reaction rate constants determined at various temperatures and using Eq. (5), the kinetic parameters have been determined and reported Table 3. Except the last case that is discussed later, the determined values of the activation energies are in the same order. For the sake of comparison, the values determined here through the Arrhenius method and the use of a kinetic model are plotted in Fig. 5 alongside values determined earlier through isoconversional method. Values are in good agreement for the α-range they have in common. The surface treatment with HF solution has led to lower values for the kinetic parameters. The real meaning of the change of the determined activation energies is difficult to firmly establish due to their low difference (it is commonly held that the incertitude of this kind of determination is roughly 10%). The lessening might nevertheless be the result of the loss of the native oxide under the effect of HF treatment. As shown in Fig. 4, the transformations are retarded after HF treatment and this is brought out by the decrease of the pre-exponential factor, which might be the expression of a drop of the nucleation rate. The values determined for the event *ix*2 for HF60 are unconnected with the others and have probably no physical meaning. The corresponding diffractogram shown in Fig. 6b and c points the coexistence of two main phases (The Zr_2Ni- and the Zr_3Al_2-based phase) and therefore the possibility to determine kinetic parameters is illusive without more information. It is nevertheless noteworthy that the peculiarity of the products obtained for HF60 after *ix*2 is highlighted by diverging determined kinetic parameters (Table 3).

The analysis of the data for *ix*E, Zr_3Al_2 formation, is not detailed here because currently inconclusive. It is actually not possible to describe its experimental master plot with any existing theoretical master plot. It should be possible to ascribe the A3 model to it by discarding the last part of the measured enthalpy (roughly the last 15%). In the same way the plots of $y(\alpha)$ have an "abnormal" shape. The same correction leads to a plot that superimposes with the plots of the *ix*2 events. Nevertheless there is currently no obvious reason to valid such correction.

4.2.3. *On the influence of surface nucleation*

The modification of the surface of the metallic glass $Zr_{59}Ti_3Cu_{20}Al_{10}Ni_8$ through hydrofluoric acid (HF) treatment leads to a modification of its thermal crystallisation behaviour upon heating. In outline, the increase of the HF treatment intensity leads to a change of the intermediates (from quasicrystalline-/Zr_2Ni- to a Zr_3Al_2-based phase) but not of the final phase (Zr_2Cu, whatever the case considered). The DSC scans, isothermal or at constant heating rate, corresponding to the formation of the intermediates evolve from two exothermic steps to a single one. On closer examination, it is found that the influence of the HF treatment process on the crystallisation is complex and manifold.

The first discussion is of the lighter HF treatment (corresponding to the sample etched for 60 s, HF60). In this case, like for the as-spun sample (AS), the crystallisation process starts in the range ~700–750 K by a two-step process. For the first step, corresponding to the isothermal event *ix*1, the quasicrystalline phase formed is the same for both samples (AS/HF60) in spite of different apparent kinetic processes (see, *e.g.* Fig. 10a). The situation for the second step, isothermal event *ix*2, is the exact opposite. The phases formed are not similar (a Zr_2Ni- alone or with a Zr_3Al_2-based phase) despite similar apparent kinetic processes (see, *e.g.* Fig. 10c).

It is obvious from Fig. 6a that the quasicrystalline phase formed is the same irrespective of the treatment and thus of the surface state. The lightly HF-modified surface leads to an apparent homogenisation of the process in the sense that the activation energy (obtained from isoconversional method) is almost constant along the whole α range, especially compared to the untreated sample (see Fig. 5). Moreover, a very good fit between the HF60 data and the A2 reaction model for the whole α range is observed. That is not the case for the AS data (Fig. 11 and Table 2). The qc-formation process also appears slowed down for the 60 s etched surface in comparison to the untreated surface (see Fig. 4 and Table 2). This can be understood in terms of nucleation. The light HF treatment would diminish the effectiveness of nucleation, in particular surface nucleation that would drive the global process. In addition, the sharpest peak obtained by XRD for HF60, the slight increase of the crystallisation temperature T_{x1} with the duration of the HF treatment (before the change of regime) as well as the diminution of the pre-exponential factor (see Table 3) are compatible with a formation process globally unchanged but with a drop in its nucleation rate.

On the other hand, the behaviour of the $y(\alpha)$ and $z(\alpha)$ functions (see Fig. 10) displays the quasicrystalline phase formation is intrinsically a complex process that cannot be "simply" described by the JMA-model. The reason(s) for such a deviation is(are) not fully understood yet but we can mention there is strong correlation with the presence (or not) of surface oxide after the isothermal annealing. By XRD (not detailed here), the stable monoclinic α-ZrO_2 and mainly the metastable tetragonal β-ZrO_2 are detected indicating that thermal oxidation have taken place during the treatment, due to the presence of residual oxygen during DSC runs. For HF60, the final oxide fraction has been the same for the temperatures of 705 and 715 K and has dropped considerably for the isothermal treatment at 725 K. This can be understood as follows: the quasicrystalline phase and the α/β-ZrO_2 compete for the same surface nucleation sites but do not have the same nucleation rate. In other words, ZrO_2 would have the lowest activation energy and thus predominate at lower temperature while at 725 K, the rate for the quasicrystalline phase becomes much higher than the rate for the zirconium oxides (and $z(\alpha)$ matches the JMA-model). On the contrary, for AS there is always the presence of zirconium oxides beside the quasicrystalline phase and the behaviour of $z(\alpha)$ never matches the JMA-model. It is also noteworthy that for the samples leading to the sole formation of Zr_3Al_2, there is formation of neither quasicrystalline nor zirconium oxides phases. This confirms the sites for Zr_3Al_2 and quasicrystalline phases are not the same and also that quasicrystals and ZrO_2 are in competition. The strong interplay between the quasicrystals formation, the thermal surface re-oxidation and the adequacy with the JMA-model is also highlighted by the continuous substitution of Zr by Ti (at least up to 6% of Ti) that leads during isothermal annealing to a continuous relative increase of the fraction of α/β-ZrO_2, a diminution/vanishing of the quasicrystalline phase and a simultaneous "increased remoteness" from the JMA-model (continuous decrease of the parameter α_Z^*, Eq. (10b)).

In the course of the crystallisation of the samples considered, there is after the formation of the quasicrystalline phase a second step, isothermal event *ix*2, leading to the formation of a Zr_2Ni-based phase. For the event *ix*2, there is apparently no influence of the surface upon the kinetic process. A reason for the apparent lower sensitivity of the Zr_2Ni-phase to surface modification might be a sign that the nucleation of the Zr_2Ni does not occur on the surface but is linked to the previous phase formed and the reactions appear to be consecutive ones. There is, indeed, invariance of $y(\alpha)$ and $z(\alpha)$ functions which are also in conformity with the

JMA-model (see Fig. 10). Moreover, good fits between the experimental master plot and the A3 reaction model for the whole α range have been obtained, the main difference being a slower reaction rate for the HF-treated sample. There is also a relative good stability of *Ea* calculated by isoconversional method (not shown). Nevertheless, the determination of *Ea* through the Arrhenius equation for the HF-treated sample is problematic and without physical meaning (see Table 3). This is associated with the presence beside the expected qc- and Zr_2Ni phases of an additional phase, namely Zr_3Al_2, as detected by XRD after 10 min of isothermal treatment (Fig. 6). It is noteworthy that the formation of this second phase cannot easily be perceived with the kinetic data, probably because the qc/Zr_2Ni and Zr_3Al_2 nucleation are spatially isolated and the volume fraction involved in the formation of Zr_3Al_2 is probably very low compared to the one of Zr_2Ni. The diffracting intensity is more important for Zr_3Al_2 which is thus more easily detected than Zr_2Ni, due to the narrower full width at half maximum (fwhm) for Zr_3Al_2 in the present case (0.278° *vs.* 1.272° for Zr_2Ni for peaks at ~45°).

In summary, it appears that the surface crystallisation, especially through surface nucleation, of the metallic glass $Zr_{59}Ti_3Cu_{20}Al_{10}Ni_8$, plays a big role in the crystallisation process. In particular, it exists (at least) two different pathways during heating. Both ends with the formation of Zr_2Cu but the first step is the formation of either quasicrystals or Zr_3Al_2. The two reactions are parallel reactions but not in competition, in the sense that the nucleation sites are not the same and are spatially isolated. The nucleation of quasicrystals appears to be favoured by the flat areas while the concave regions favour Zr_3Al_2. In addition, the native oxide layer acts also on the nucleation process of each phases. Clearly, its presence hinders the formation/development of Zr_3Al_2. The nucleation of Zr_3Al_2 seems “activated” and “accelerated” by its removal. The curved in (concave) regions are known to increase the atomic mobility and faster atomic transport occurs on oxide-free surface, therefore we infer the surface atomic mobility is a main factor affecting the eventual formation of Zr_3Al_2. On the other hand, the influence of the native surface oxide on the quasicrystalline phase formation is more subtle. Its removal leads on a process slowed down, which can be seen as a diminution of the effectiveness of the nucleation process (change in site density, drop in nucleation rate, etc.). Nevertheless, other explanation cannot be ruled out (change in the growth velocity, influence of other material features generated by the oxide removal treatment).

5. Conclusion

This report shows that the surface of a metallic glass ($Zr_{59}Ti_3Cu_{20}Al_{10}Ni8$) plays an important role on its devitrification behaviour. The surface of the material was modified by means of hydrofluoric acid (HF) etching. The subsequent changes of the devitrification process have been followed by DSC mainly under isothermal conditions and by XRD analysis of the (quasi-)/crystalline products. The DSC results show that the nucleation-growth process is the mechanism of the crystallisation; nevertheless, it cannot be described by the JMA-model in all the experimental situations. Therefore, the results have been analysed using the kinetic models based on nucleation/growth mechanism, namely A2 or A3. Taking heed of all these DSC behaviour analyses, a process strongly affected by the surface nucleation is sketched. The structural analyses confirm this. In particular, the first appearing phase(s): quasicrystalline, Zr_2Ni- or Zr_3Al_2-based, are strongly dependent on the (chemical and/or topological) surface state. The topological nature is assumed the primary factor. The curved in (concave) areas, brought about by the initial preparation technique (melt-spinning) or also by corrosion, lead to the formation of a Zr_3Al_2-based phase, whereas the flat flawless areas favour the “couple” qc/Zr_2Ni. On the other hand, the presence of an oxide surface layer cancels the effects of the topological differences out. The oxide surface layer would hinder the nucleation process of Zr_3Al_2 in the concave regions. This layer also affects the nucleation of the quasicrystalline phase on the surface. The quasicrystalline phase formation is hampered by its removal leading to an apparent nucleation process less effective. The quasicrystalline phase formation is also in competition with the parallel formation of ZrO_2 due to thermal re-oxidation during the DSC experiments. The nature of the developing non-glassy phase(s) is not (only) governed by the internal organisation of the glass; the possibility (or not) of certain phases to nucleate on the surface is of key importance. The results give additional insight into the devitrification process of a glassy metallic alloy and stress on the role of the surface.

Acknowledgements

Thanks are due for experimental assistance to H. Bußkamp for oxygen analyses, M. Frey for the preparation of pre-alloys, B. Jerliu for the help in preparation of some samples, P.F. Gostin and N. Scheerbaum for SEM-EDX analyses, C. Mickel for TEM analyses and A. Voß for ICP-OES analyses.

References

[1] A. Inoue, Acta Mater. 48 (2000) 279–306.
[2] A. Takeuchi, A. Inoue, Mater. Trans. 46 (2005) 2817–2829.
[3] L.Q. Xing, J. Eckert, W. Löser, L. Schultz, D.M. Herlach, Philos. Mag. A 79 (1999) 1095–1108.
[4] J.G. Wang, B.W. Choi, T.G. Nieh, C.T. Liu, J. Mater. Res. 15 (2000) 798–807.
[5] A.A. Kündig, J.F. Löffler, W.L. Johnson, P.J. Uggowitzer, P. Thiyagarajan, Scripta Mater. 44 (2001) 1269–1273.
[6] E. Pekarskaya, J.F. Loffler, W.L. Johnson, Acta Mater. 51 (2003) 4045–4057.
[7] A.A. Kündig, M. Ohnuma, T. Ohkubo, K. Hono, Acta Mater. 53 (2005) 2091–2099.
[8] S. Scudino, J. Eckert, C. Mickel, L. Schultz, J. Non-Cryst. Solids 351 (2005) 856–862.
[9] U. Kühn, K. Eymann, N. Mattern, J. Eckert, A. Gebert, B. Bartusch, L. Schultz, Acta Mater. 54 (2006) 4685–4692.
[10] A. Inoue, T. Zhang, T. Masumoto, Mater. Trans., JIM 31 (1990) 177–183.
[11] T. Zhang, A. Inoue, T. Masumoto, Mater. Trans., JIM 32 (1991) 1005–1010.
[12] A. Inoue, T. Zhang, N. Nishiyama, K. Ohba, T. Masumoto, Mater. Trans., JIM 34 (1993) 1234–1237.
[13] L.Q. Xing, P. Ochin, Acta Mater. 45 (1997) 3765–3774.
[14] X.H. Lin, W.L. Johnson, W.K. Rhim, Mater. Trans., JIM 38 (1997) 473–477.
[15] A. Inoue, T. Shibata, T. Zhang, Mater. Trans., JIM 36 (1995) 1420–1426.
[16] T. Zhang, A. Inoue, Mater. Trans., JIM 39 (1998) 857–862.
[17] T.H. Kim, A.K. Gangopadhyay, L.Q. Xing, G.W. Lee, Y.T. Shen, K.F. Kelton, A.I. Goldman, R.W. Hyers, J.R. Rogers, Appl. Phys. Lett. 87 (2005) 251924.
[18] K.F. Kelton, F. Spaepen, Acta Metall. 33 (1985) 455–464.
[19] U. Köster, Mater. Sci. Eng. 97 (1988) 233–239.
[20] A. Calka, A.P. Radliński, Mater. Sci. Eng. 97 (1988) 241–246.
[21] J.R. Scully, A. Gebert, J.H. Payer, J. Mater. Res. 22 (2007) 302–313.
[22] B. Vishwanadh, G.J. Abraham, Jagannath, S. Neogy, R.S. Dutta, G.K. Dey, Metall. Mater. Trans. A 40A (2009) 1131–1141.
[23] E. Fleury, S.M. Lee, H.S. Ahn, W.T. Kim, D.H. Kim, Mater. Sci. Eng. A 375–377 (2004) 276–279.
[24] G. Partridge, P.W. McMillan, Glass Technol. 15 (1974) 127–133.
[25] A. Gebert, N. Ismail, U. Wolff, M. Uhlemann, J. Eckert, L. Schultz, Intermetallics 10 (2002) 1207.
[26] U. Wolff, A. Gebert, J. Eckert, L. Schultz, J. Alloys Compd. 346 (2002) 222–229.
[27] S. Spriano, M. Baricco, C. Antonione, E. Angelini, F. Rosalbino, P. Spinelli, Electrochim. Acta 39 (1994) 1781–1786.
[28] T. Katona, A. Molnár, J. Catal. 153 (1995) 333–343.
[29] E. Angelini, C. Antonione, M. Baricco, S. Daolio, M. Fabrizio, F. Rosalbino, Rapid Commun. Mass Spectrom. 14 (2000) 800–807.
[30] K. Brunelli, M. Dabalà, R. Frattini, G. Sandona, I. Calliari, J. Alloys Compd. 317–318 (2001) 595–602.
[31] A.P. Radliński, A. Calka, J. Appl. Phys. 64 (1988) 423–426.
[32] M. Varga, G. Mulas, G. Cocco, A. Molnár, J. Therm. Anal. Calorim. 56 (1999) 305–310.
[33] U. Köster, L. Jastrow, J. Metastable Nanocryst. Mater. 20–21 (2004) 407–414.
[34] K. Mondal, U.K. Chatterjee, B.S. Murty, J. Alloys Compd. 433 (2007) 162–170.
[35] E.D. Zanotto, V.M. Fokin, Philos. Trans. R. Soc. A 361 (2003) 591–613.
[36] A. Gebert, J. Eckert, L. Schultz, Acta Mater. 46 (1998) 5475–5482.
[37] F.J. Gotor, J.M. Criado, J. Málek, N. Koga, J. Phys. Chem. A 104 (2000) 10777–10782.
[38] A. Khawam, D.R. Flanagan, J. Phys. Chem. B 110 (2006) 17315–17328.

[39] J. Burke, The Kinetics of Phase of Phase Transformation in Metals, 1st ed., Pergamon Press, Oxford, 1965.

[40] J.W. Christian, The Theory of Transformation in Metals and Alloys, 2nd ed., Pergamon Press, Oxford, 1975.

[41] J. Málek, Thermochim. Acta 355 (2000) 239–253.

[42] K.N. Lad, R.T. Savalia, A. Pratap, G.K. Dey, S. Banerjee, Thermochim. Acta 473 (2008) 74–80.

[43] J. Wang, H.C. Kou, J.S. Li, X.F. Gu, L.Q. Xing, L. Zhou, J. Alloys Compd. 479 (2009) 835–839.

[44] N. Mattern, U. Kühn, H. Hermann, H. Ehrenberg, J. Neuefeind, J. Eckert, Acta Mater. 50 (2002) 305–314.

[45] U. Köster, U. Schünemann, in: H.H. Liebermann (Ed.), Rapidly Solidified Alloys, Marcel Dekker Inc., New York, 1993, pp. 303–338.

[46] J. Eckert, N. Mattern, M. Zinkevitch, M. Seidel, Mater. Trans., JIM 6 (1998) 623–632.

[47] C.G. Wilson, F.J. Spooner, Acta Cryst. 13 (1960) 358–359.

[48] A.R. Yavari, A. Le Moulec, A. Inoue, W.J. Botta, G. Vaughan, A. Kvick, Mater. Sci. Eng. A 304–306 (2001) 34–38.

[49] Y. Li, K. Georgarakis, S. Pang, C. Ma, G. Vaughan, A.R. Yavari, T. Zhang, Intermetallics 17 (2009) 231–234.

[50] K.F. Kelton, in: H. Li, C.S. Ray, D.M. Strachan, R. Weber, Y. Yue (Eds.), Melt Chemistry, Relaxation, and Solidification Kinetics of Glasses: Ceramic Transactions, vol. 170, American Ceramic Society, Westerville, OH, 2005, pp. 147–162.

[51] A. Calka, A.P. Radliński, J. Mater. Res. 3 (1988) 59–66.

[52] G. He, G.L. Chen, Z. Bian, Intermetallics 8 (2000) 481–485.

[53] S. Venkataraman, H. Hermann, C. Mickel, L. Schultz, D.J. Sordelet, J. Eckert, Phys. Rev. B 75 (2007) 104206.

[54] T. Ozawa, J. Therm. Anal. Calorim. 82 (2005) 687–690.